JACS
JOURNAL OF THE AMERICAN CHEMICAL SOCIETY
pubs.acs.org/JACS
Article

Free Volume Element Sizes and Dynamics in Polystyrene and Poly(methyl methacrylate) Measured with Ultrafast Infrared Spectroscopy

Sebastian M. Fica-Contreras, David J. Hoffman, Junkun Pan, Chungwen Liang, and Michael D. Fayer*

Cite This: J. Am. Chem. Soc. 2021, 143, 3583−3594

ABSTRACT: The size, size distribution, dynamics, and electrostatic properties of free volume elements (FVEs) in polystyrene (PS) and poly(methyl methacrylate) (PMMA) were investigated using the Restricted Orientation Anisotropy Method (ROAM), an ultrafast infrared spectroscopic technique. The restricted orientational dynamics of a vibrational probe embedded in the polymer matrix provides detailed information on FVE sizes and their probability distribution. The probe's orientational dynamics vary as a function of its frequency within the inhomogeneously broadened vibrational absorption spectrum. By characterizing the degree of orientational restriction at different probe frequencies, FVE radii and their probability distribution were determined. PS has larger FVEs and a broader FVE size distribution than PMMA. The average FVE radii in PS and PMMA are 3.4 and 3.0 Å, respectively. The FVE radius probability distribution shows that the PS distribution is non-Gaussian, with a tail to larger radii, whereas in PMMA, the distribution is closer to Gaussian. FVE structural dynamics, previously unavailable through other techniques, occur on a ∼150 ps time scale in both polymers. The dynamics involve FVE shape fluctuations which, on average, conserve the FVE size. FVE radii were associated with corresponding electric field strengths through the first-order vibrational Stark effect of the CN stretch of the vibrational probe, phenyl selenocyanate (PhSeCN). PMMA displayed unique measured FVE radii for each electric field strength. By contrast, PS showed that, while larger radii correspond to unique and relatively weak electric fields, the smallest measured radii map onto a broad distribution of strong electric fields.

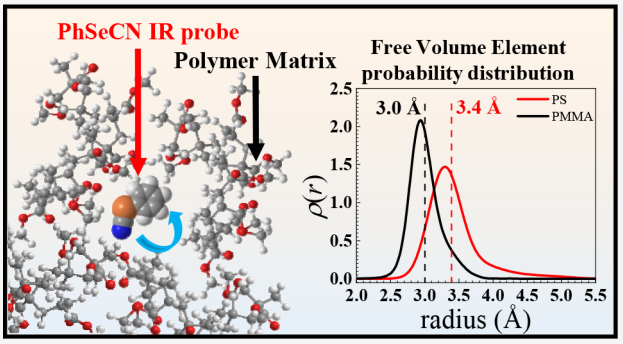

1. INTRODUCTION

The study of free volume in glassy polymeric matrices has been the subject of a large number of research studies. Various experimental and computational techniques have been developed to elucidate the characteristics and behaviors of free volume.[1−6] Understanding free volume in glassy polymers is of substantial importance, as free volume determines many of the macroscopic properties of polymeric materials. Specifically, free volume plays a key role in transport properties,[7,8] polymer mechanics,[2,9,10] viscosity,[11] thermal response,[12,13] and electrical properties.[14] However, the small size of individual free volume elements (FVEs), on the order of a few angstroms in radius, makes measuring FVE sizes and size distributions very challenging.

Free volume results from the imperfect packing of polymer chains. Below the glass transition temperature (T_g), the polymer chains become effectively locked in position.[15,16] The polymer structure is unable to undergo sufficient rearrangements to pack efficiently.[2] Therefore, the system becomes trapped in high-energy non-equilibrium configurations, where full chain dynamics are effectively eliminated.[2,7,15,16] The imperfect packing that results from the non-equilibrium configurations leaves void spaces scattered throughout the polymeric matrix.[16] Each individual pocket of void space is an FVE.[1−3] In the glassy state, the polymer matrix undergoes subtle structural rearrangements, executing an exceedingly slow evolution toward thermal equilibrium, i.e., physical aging.[2,17] However, the dramatic slowing of cooperative chain mobility below T_g prevents the system from reaching its lowest free energy state.[2]

Because polymers can still undergo small local structural rearrangements in the glassy state, FVEs are not a completely static component of the polymeric system. Structural dynamics occur on a wide range of time scales. The polymer side groups and short sections of polymer chains can undergo fast motions on the order of a few picoseconds to hundreds of picoseconds.[18] Over a variety of macroscopic time scales (up

Received: December 28, 2020
Published: February 25, 2021

https://dx.doi.org/10.1021/jacs.0c13397
J. Am. Chem. Soc. 2021, 143, 3583−3594

to years or longer), the polymer ages due to intrinsic and extrinsic factors, and its total free volume content can change.[2,12,19,20] As a result, a more nuanced understanding of free volume is important. In a static view, free volume is defined as any space not occupied by polymer chains.[2,16] In a dynamic view, FVEs have structures that undergo shape and position fluctuations about an average value.[18]

Previously, we introduced a new technique for measuring polymer matrix FVE sizes, size distributions, and dynamics using ultrafast infrared spectroscopy.[18] The technique is called Restricted Orientation Anisotropy Method (ROAM), and it was first demonstrated on a poly(methyl methacrylate) (PMMA) film with embedded phenyl selenocyanate (PhSeCN) as the vibrational probe, where the reporting vibration is the CN stretching mode. ROAM uses an ultrafast infrared polarization-selective pump−probe (PSPP) experiment to observe the orientational relaxation dynamics of PhSeCN in polymer FVEs.[21] Femtosecond laser pulses and the long vibrational excited-state lifetime of PhSeCN (hundreds of picoseconds), allow PSPP to resolve molecular dynamics as fast as 0.5 ps and as slow as ∼1 ns. Time-resolved ultrafast dynamics of FVEs are an attribute that has not been previously accessible with experimental techniques. These dynamics correspond to FVE restructuring that results from fast mesoscopic polymer chain motions.[18]

The structural heterogeneity of FVEs causes inhomogeneous broadening of the probe's CN stretch infrared (IR) absorption spectrum. The angular range of reorientation of PhSeCN is restricted by the inner wall of the FVE, and the extent of restriction depends on the FVE size. As the size increases, PhSeCN can sample a wider range of angles. As a result, in each sub-ensemble of FVEs of the same size, PhSeCN molecules display distinct orientational dynamics. Measurement of the restricted orientational dynamics as a function of the frequencies across the inhomogeneously broadened CN vibrational absorption line yields strongly frequency-dependent anisotropic decays.[18] This is the key to the ROAM analysis of the FVE size distribution. Parameterization of the frequency-dependent anisotropy decays (orientational relaxation) using the well-established wobbling-in-a-cone model enables the extraction of cone angles that quantify the extent of angular motion of the vibrational probe.[22−24] These angles are converted to FVE radii using the molecular dimensions of the PhSeCN probe. Because different FVE sizes produce different degrees of restriction on the probe's orientational motion, the distribution of observed cone angles yields the distribution of FVE sizes. Further, applying first-order vibrational Stark effect analysis to the nitrile probe gives the electric field strengths experienced by the vibrational probes inside FVEs as a function of FVE size.[18,25]

Previously, FVE sizes in polymer matrices have been obtained most robustly from positron annihilation lifetime spectroscopy (PALS),[4,5,26−33] as well as from the emission of photoisomerizable photochromic fluorophores,[19,34,35] and the chemical shift of ^{129}Xe in nuclear magnetic resonance experiments.[1,36] However, these techniques do not provide access to the fast time-dependent behavior of FVEs, nor are they able to report on their electrostatic characteristics.

Here, we present a comparative study of the FVE sizes, size distributions, FVE topography fluctuation time scales, and electrostatic properties of PS and PMMA using ROAM. PMMA and PS have been widely studied in the literature.[1,2,6,28,32,34] The measurements made on PS and PMMA demonstrate that ROAM is sensitive to polymer structure at the sub-angstrom length scale. PS was found to have larger FVEs and a broader FVE size distribution than PMMA, and very similar time scales for the FVE structural fluctuations. Using the first-order vibrational Stark effect analysis, it was found that in PS, small FVEs are associated with a broad distribution of strong electric fields, whereas large FVEs are associated with weaker and a narrower distribution of electric field strengths. In contrast, PMMA displays closer to a one-to-one relation between experimentally measured FVE radius and electric field strength over a wider range of radii.

Previously, we reported a method for extracting the FVE radii distribution based on a limited set of data for PMMA.[18] The study of PS and additional PMMA data presented here demonstrate that the method used previously is not general and is incorrect, except in possible special cases that do not occur in PS or PMMA. The new results show that the prior simple analysis method, when applied to the expanded data set, does not describe the full distribution of FVE radii in PMMA. Here, we present new experimental investigations of PS and PMMA and a rigorous theoretical framework, which are critical for the development of the general method for extracting the distribution of FVE radii from the ROAM observables. Using the probe's absorption spectrum and the frequency-dependent radii measurements, a characteristic FVE radius probability distribution can be determined. Applying this analysis to PS and PMMA revealed that both distributions are somewhat non-Gaussian with tails to larger radii, but the effect is much more pronounced in PS. These results provide new details of the microscopic intricacies of polymer structures and insights into polymer physics.

2. EXPERIMENTAL PROCEDURES

2.1. Sample Preparation. PS and PMMA (MW 350 000 Da) were purchased from Sigma-Aldrich and used without further purification. The same high molecular weight for both polymers was used to avoid plasticizing effects from a high concentration of chain end-groups. It has been shown that FVE sizes change as a function of molecular weight, when the molecular weight is low.[32,33] 350 kDa was chosen as it is sufficiently high that the FVE properties should be independent of molecular weight, and it results in a low concentration of end-groups, ensuring investigation of bulk FVE characteristics. Nonetheless, using identical MW for PS and PMMA ensures that all observed differences in FVE sizes and distributions only result from differences between the two polymers.

Films were prepared by a drop solvent-cast method. Using the polymer's density (PMMA: 1.18 g/mL, and PS: 1.05 g/mL), an appropriate mass of polymer was dissolved in excess chloroform (∼200 mg/mL) to create a film of thickness 250 μm for PS and 100 μm for PMMA, and of area 3 × 3 in. PhSeCN (Sigma-Aldrich) was dissolved in this solution at a concentration of 5 mol % in PS and 2.5 mol % in PMMA with respect to the monomeric unit of the polymers. The resulting solution was deposited onto a leveled glass substrate with glass walls to contain the solution, and the excess chloroform was allowed to slowly evaporate overnight. The top of the glass box was covered to slow down solvent evaporation and avoid the formation of bubbles in the film, which lower the films' optical quality. Once the solvent was evaporated, a film of sound structural integrity and high optical quality was peeled off the glass substrate. The remaining solvent was removed by drying the films in a vacuum oven (Thermo Scientific Iso Vac Oven model 282) at <100 mTorr. Both films were heated for 7.5 days at 50 °C, followed by 1.5 days at 90 °C for PS, and 6.5 days at 90 °C for PMMA. The solvent and vibrational probe contents were determined by ^{1}H nuclear magnetic resonance (NMR) spectroscopy (see below). A 1 cm^2 piece was then cut from the film,

https://dx.doi.org/10.1021/jacs.0c13397
J. Am. Chem. Soc. 2021, 143, 3583−3594

sandwiched between two calcium fluoride (CaF_2) windows, and placed in a temperature-controlled copper cell.

2.2. NMR Measurements. ^{1}H NMR was used to quantify the solvent and vibrational probe content of the films. Solvent and probe concentration-dependent experiments were conducted to determine that the small amount of residual solvent and the concentration of the IR probe did not affect the results of the ROAM measurements. The complete details of the NMR characterization and concentration-dependent experiments are presented in the Supporting Information (SI).

2.3. FTIR Measurements. FT-IR spectra of both samples were collected using a Thermo-Fisher iS50 infrared spectrometer using a resolution of 0.24 cm^{-1}. Spectra of probe-free PMMA and PS were used to perform background subtraction to yield the absorption spectrum of PhSeCN in each sample.

2.4. Ultrafast Infrared Equipment. A detailed description of an analogous instrument has been provided previously.[37,38] Briefly, a Ti:sapphire oscillator seeding a regenerative amplifier was used to produce 800 nm femtosecond pulses with 2 mJ of energy per pulse and 3 kHz repetition rate. The output from the regenerative amplifier is converted from 800 nm to 4.6 μm (30 μJ and 3 kHz repetition rate) using a home-built optical parametric amplifier (OPA). The 4.6 μm pulses have a bandwidth of 100 cm^{-1} and are near transform-limited. The mid-IR OPA output is tuned to be resonant with the vibrational frequency of the CN stretch of PhSeCN.

In the PSPP experiment, the IR pulse is split into a strong pump pulse (~90% intensity) and a weak probe pulse (~5% intensity). Pump and probe overlap in the sample, and their separation in arrival time is precisely controlled. The pump is directed through a germanium acousto-optic modulator (AOM) for pulse shaping, which is used to block the frequencies of light resonant with the PhSeCN nitrile stretch in every other pump pulse[39] and for phase cycling, which reduces scattered light. The probe is directed down a mechanical delay stage with a delay range of ~2 ns. Before reaching the sample, the polarization of the pump pulse is rotated with a half wave plate and polarizer +45° relative to the probe pulse. A polarizer on a computer-controlled rotation stage is used to resolve the probe polarization after the sample at +45° and −45°, for parallel and perpendicular measurements relative to the pump polarization, respectively. The probe pulse is then frequency resolved using a monochromator and a 32-pixel mercury cadmium telluride (MCT) array detector. An additional horizontal polarizer is placed after the rotating polarizer to match the detected probe intensity in each polarization on the MCT array. The signal is the difference in transmitted probe intensity between shots with the pump on and shots with the resonant pump blocked. The time evolution of the parallel ($I_{\parallel}$) and perpendicular ($I_{\perp}$) pump−probe signals is obtained by increasing the time delay, t, between pump and probe pulses, using the mechanical delay stage and the following equations:[21,40]

$$I_{\parallel} = P(t)(1 + 0.8C_2(t))$$
$$I_{\perp} = P(t)(1 - 0.4C_2(t)) \quad (1)$$

$P(t)$ is the isotropic signal, i.e., the CN vibrational excited-state population lifetime. $C_2(t)$ is the second Legendre polynomial orientational correlation function.

3. RESULTS AND DISCUSSION

3.1. Restricted Orientation Anisotropy Method (ROAM). The normalized linear absorption spectra of PhSeCN in MW 350 kDa PS and PMMA, fit on the high-frequency sides of the lines with Gaussian functions, are presented in Figure 1. The Gaussian fits were extended to the low-frequency sides of the lines. The absorption spectrum of PhSeCN in PS is centered at 2155.4 ± 0.1 cm^{-1}, and it has a full-width at half-maximum (FWHM) of 8.4 ± 0.1 cm^{-1}. In PMMA, the spectrum is centered at 2154.9 ± 0.1 cm^{-1} and has a FWHM of 10.5 ± 0.1 cm^{-1}. These parameters are consistent with the

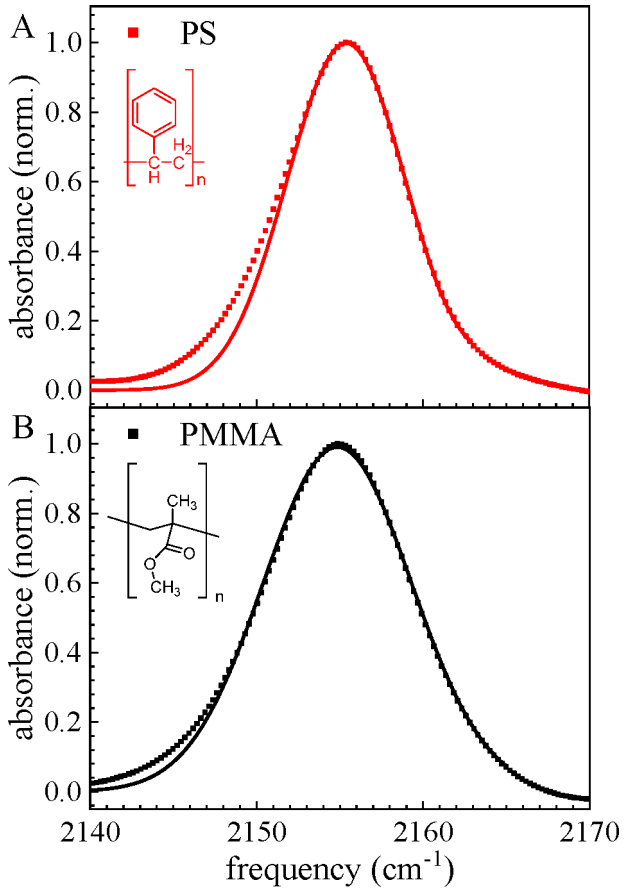

Figure 1. Linear FT-IR spectra of the CN stretch of PhSeCN in (A) PS and (B) PMMA. The points are the experimental data. The solid curves are Gaussian fits to the high-frequency sides of the spectra and then extended to the low-frequency sides. The PS spectrum deviates substantially from a Gaussian line shape, while that for PMMA is much closer to Gaussian. The spectrum of PhSeCN in PS is shifted to a higher frequency and has a narrower FWHM compared to the spectrum in PMMA.

absorption spectra of PhSeCN in other non-hydrogen bonding environments.[41,42] In the absence of hydrogen bonding, nitriles shift their absorption maximum to higher frequency with decreasing solvent polarity.[25,43] Therefore, the blue-shifted absorption spectrum in PS compared to PMMA is anticipated, although based on the magnitude of spectral shifts in liquids, the difference is somewhat smaller than might be expected given the bulk polarity of the two polymers. The inhomogeneous absorption line of PhSeCN determines the range of frequencies over which it is possible to extract anisotropic decay curves with high signal quality. A 9 cm^{-1} range, roughly corresponding to the FWHM of the absorption line widths, was used for the analysis.

It can be seen that the Gaussian fit is able to reproduce the absorption spectrum of PhSeCN in PMMA reasonably well, with the exception of a small deviation on the low-frequency side of the line beginning at ~2148 cm^{-1}. In contrast, for PS the Gaussian fit begins to fail on the red side of the line close to the spectrum's center at ~2153 cm^{-1}. The inhomogeneous absorption line results from the distribution of local environments in the polymer matrix that gives rise to a distribution of electric fields and therefore to a distribution of frequencies. The spectra show that the CN of PhSeCN in PMMA FVEs experience close to a Gaussian distribution of local electric

https://dx.doi.org/10.1021/jacs.0c13397
J. Am. Chem. Soc. 2021, 143, 3583−3594

fields, while in PS the distribution deviates substantially from Gaussian.

3.1.1. Polarization-Selective Pump−Probe (PSPP) Infrared Experiment. PSPP experiments measure the orientational relaxation and vibrational lifetime of the probe molecules embedded in the polymer matrix.[21,23] The orientational relaxation is very sensitive to the local structures around the probe and to the local polymer dynamics, as time-dependent changes in the local polymer structure can enable a greater extent of orientational relaxation. Combinations of $I_{\parallel}$ and $I_{\perp}$ (eq 1) provide an expression for the excited-state lifetime, $P(t)$, and the orientational dynamics, i.e., the anisotropy $r(t)$, as follows:

$$P(t) = \frac{1}{3}(I_{\parallel} + 2I_{\perp})$$

$$r(t) = \left(\frac{I_{\parallel} - I_{\perp}}{I_{\parallel} + 2I_{\perp}}\right) = 0.4C_2(t) \quad (2)$$

$C_2(t) = 1$ at $t = 0$. Therefore, the maximum possible value of the measured anisotropy, $r(t)$, is 0.4. In practice, the observed initial value of $r(t)$ is lower than 0.4, which results from inertial dynamics that occur on time scales faster than can be resolved by the instrument. The importance of this inertial motion will be discussed further below.

In the PS and PMMA systems, the population relaxation of PhSeCN is described by a frequency-independent single-exponential decay with time constants (lifetime) 437 ± 0.4 ps in PS and 434 ± 0.6 ps in PMMA (see SI). However, for the purpose of studying FVE sizes, orientational relaxation is the main observable investigated.

The frequency-dependent anisotropy decays, $r(t)$ (orientational relaxation, eq 2), are shown in Figure 2 for both polymers. The solid lines through the data are fits using eq 3 and will be discussed in detail below. All curves are biexponential decays to frequency-dependent offsets (constant values). The parameters from the fits using this functional form are presented in Tables S1 and S2 (see SI). For example, at the center frequency of the spectrum in PMMA (2154 cm^{-1}), the two decay constants are 7.1 ± 1.0 ps (amplitude 0.030 ± 0.002) and 156 ± 26 ps (amplitude 0.03 ± 0.002) with a long time offset of amplitude 0.290 ± 0.001. For PS, the corresponding numbers are 7.6 ± 1.0 ps (0.060 ± 0.004) and 170 ± 26 ps (0.060 ± 0.003) with a long time offset of 0.210 ± 0.002. An important aspect of the decays is the large separation in time scales, which makes it possible to extract the amplitudes of each decay accurately. The frequency dependence of the decays in Figure 2 is unusual, as anisotropy decays are generally frequency-independent except for a few chemical systems with strong directional hydrogen bond interactions.[44,45] The observation of frequency-dependent orientational dynamics demonstrates that the distribution of chemical environments in the polymer matrices are distinguishable by the probe molecule's frequency and persistent throughout the experiment. Therefore, the sub-ensembles of PhSeCN found in each micro-environment display distinct orientational dynamics. As discussed in detail below, these distinguishable microenvironments correspond to FVEs of different sizes that contain the PhSeCN probe molecules.[18]

Equation 2 shows that the anisotropy has a maximum value of 0.4 and a minimum value of 0. The 0.4 value at $t = 0$ occurs prior to the onset of orientational dynamics. As mentioned

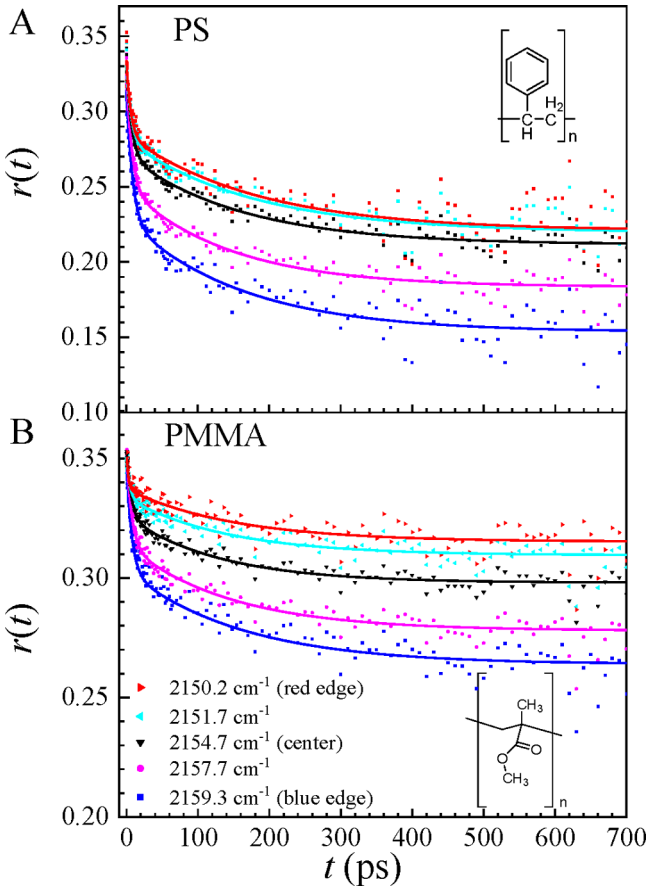

Figure 2. Anisotropy decay data (points) of PhSeCN in 350 kDa (A) PS and (B) PMMA films. Fits with eq 3 are shown as solid curves. The extent of orientational relaxation depends on the vibrational frequency of the probe molecule. At the lowest frequencies in PS, the orientational relaxation frequency dependence is much smaller than that in PMMA and that at high frequencies in PS.

above, an ultrafast inertial decay with a time constant faster than the experimental resolution (tens of femtoseconds) decreases the initial observed anisotropy below the theoretical maximum of 0.4. An anisotropy value of 0 at long time is caused by full randomization of the orientations of the vibrational probes. Therefore, a decay to an offset unambiguously indicates that the orientational motion of PhSeCN in PS and PMMA is restricted, such that the vibrational probe cannot fully randomize its orientation on a time scale comparable to the experimental time window. As will be described below, the restriction of the orientational motion is the key to extracting FVE radii.

For a given frequency, the anisotropy decays to a larger final offset in PMMA than in PS. A larger offset corresponds to a smaller sampled angular space. Thus, the orientational motion of PhSeCN is more restricted in PMMA than in PS across the entire frequency spectrum. In both systems, restriction of the orientational motion increases with decreasing vibrational frequency, i.e., the final offset increases. Further, in the high-frequency regime, the anisotropic decays for nearby frequencies are significantly different, whereas in the low-frequency regime, they tend to converge. Comparison of the anisotropy decays for frequencies 2150.2 and 2151.7 cm^{-1} shows that in PS, they coincide with each other, while there is still a small difference between them in PMMA. This

https://dx.doi.org/10.1021/jacs.0c13397
J. Am. Chem. Soc. 2021, 143, 3583−3594

convergent behavior is much more pronounced in PS than in PMMA. The reason for, and implication of this difference, is discussed below.

3.1.2. Orientational Relaxation and Extraction of FVE Radii. The well-established wobbling-in-a-cone model can be used to quantify the probe's orientational dynamics when there are steric restrictions that prevent complete orientational randomization, which occurs by simple orientational diffusion.[22−24,46] In the wobbling model, each component of the anisotropy curve is associated with a characteristic cone half-angle that quantifies the angular space the probe samples via its orientational motion. While the inertial decay is too fast to be resolved, the drop from 0.4 to the observed initial anisotropy value gives the extent of angular sampling by the inertial dynamics (inertial cone). Following the inertial decay, the probe can sample a limited range of angles, which is referred to as the first diffusive cone. A subsequent release of steric constraints, i.e., local polymer rearrangements, allows the probe to sample a larger range of angles, which is the second diffusive cone.

According to the wobbling model, the biexponential anisotropy decay to a finite final offset is described as[23]

$$C_2(t) = S_0^2(S_1^2 + (1 - S_1^2)\exp(-t/\tau_1)) \times (S_2^2 + (1 - S_2^2)\exp(-t/\tau_2)) \quad (3)$$

S_0^2, S_1^2, and S_2^2 are order parameters that are associated with the probe's inertial orientational motion, the first diffusive orientational relaxation, and the second diffusive orientational relaxation, respectively. The order parameter (obtained from the amplitude of each decay component) provides the extent of anisotropy decay associated with each process. As the biexponential decays are dependent on the probe's CN stretch frequency, these order parameters are also frequency-dependent. In eq 3, the order parameters can be identified with a characteristic angle, γ_i, where i denotes the inertial decay (0) and the first (1) and second (2) exponential decay components through eqs 2 and 3, in a manner that is model-free.[22] γ_i reflects the range of angles sampled by each process.

The wobbling-in-a-cone model describes each of the three restricted orientational processes as orientational motion in a hard-walled cone of cone half angle θ_i.[22−24,46] In the context of polymer matrices, the PhSeCN probes are encapsulated in the polymer's FVEs. When the probe undergoes orientational relaxation dynamics, it samples a particular cone half angle. The angle the probe can sample is determined by the size of the surrounding polymer FVE cage. The cone half angle, θ_i, is related to the order parameters, S_i, by

$$S_i = \frac{1}{2}\cos(\theta_i)(1 + \cos(\theta_i)) \quad (4)$$

The order parameters S_0, S_1, and S_2 provide three frequency-dependent cone half angles: θ_0, θ_1, and θ_2. Therefore, the orientational relaxation dynamics start with an inertial motion with cone half angle θ_0, having a decay time constant that is too fast to be resolved. This is followed by the first diffusive orientational relaxation process with a cone half angle θ_1 and time constant τ_1. Finally, polymer structural rearrangements (constraint release) of, for example, side groups and small chain segments, changes the available angular space, allowing the probe to undergo a second diffusive process with associated θ_2 and time scale τ_2.The frequency-dependent cone angles can be converted to length scales by considering the dimensions of the PhSeCN vibrational probe. The vibrational probe wobbles around the molecule's center of mass. The hard cones from the wobbling-in-a-cone analysis can be visualized as resulting from the collisions between the edges of the vibrational probes and the inner walls of the polymer's FVEs, thus restricting the reorientation of the probe molecules. A radius of a cylindrical volume element can then be extracted from the wobbling-in-a-cone half angle by the following expression:[18]

$$r_i = a \sin\theta_i + \Delta r \quad (5)$$

θ_i is the cone half-angle that generates a corresponding radius, r_i. The parameter Δr is the van der Waals radius of the probe's moiety that collides with the FVE surface, and a is the distance between the center of mass and the center of the probe's colliding moiety.[18] Two limiting geometries of PhSeCN were considered previously, which resulted in a small variation of ∼0.3 Å in FVE size for the measured dynamics.[18] Here, the average of the two models is used, which gives a = 3.15 Å and Δr = 1.85 Å.

The cone half angles of interest are θ_{0+1} and θ_{tot}, which are provided by the cumulative order parameters $S_{0+1} = S_0S_1$, and $S_{tot} = S_0S_1S_2$, respectively.[18] Using eq 5, θ_{0+1} and θ_{tot} provide two length scale measurements: r_{0+1} and r_{tot}. θ_{0+1} refers to angular sampling prior to constraint release ($\tau_1 \approx 10$ ps), and it determines the sizes of the FVEs (r_{0+1}). θ_{tot} is the larger total cone half angle available to the probe at longer time following constraint release ($\tau_2 \approx 150$ ps), and it results in a radius r_{tot}. It is important to emphasize that the total cone angle, while larger than the θ_{0+1}, does not result from an increase in FVE size.[18] Instead, θ_{tot} reflects fluctuations in the surface topographies of FVEs, which open new space for angular sampling while closing off other regions that have already been sampled. This angle is the total range of angles sampled by the probe, but not all of the angular space is available at the same time. r_{tot} reflects this total sampling range, which is larger than the average size of the FVEs, but does not represent an increase in FVE size.[18] Therefore, the average size of the FVEs (r_{0+1}) does not change, but polymer restructuring allows for a larger total angular space (r_{tot}) to be sampled. Analysis of the anisotropy decay data (Figure 2) was performed with the wobbling-in-a-cone model using eqs 2, 3, and 4. The parameters for the anisotropy decay curves using eq 3 can be found in the SI. The slow anisotropy decay time constants, $\tau_2 \approx 150$ ps, are very similar for PS and PMMA, indicating that the FVE shape fluctuations occur on the same time scale for the two polymers. The time scale and extent of the FVE shape fluctuations provide insights into the dynamic nature of the microstructure of free volume in polymer matrices. As the shapes fluctuate, the center locations of the FVEs are also expected to fluctuate. Thus, the positions of FVEs and the positions relative to each other are not constant, which may contribute to processes such as gas or electron transport.

The short-time instantaneous (θ_{0+1}) and long-time total (θ_{tot}) cone angles are presented in Figure 3 (left y-axis), together with their corresponding radii, r_{0+1} and r_{tot}, obtained from eq 5 (right y-axis). The frequency-dependent cone angles result in frequency-dependent FVE radii. These radii will be combined with the absorption spectrum of PhSeCN in each polymer to determine the probability distributions of the FVE radii (section 3.2). It is observed in Figure 3 that the cone angles, and therefore their corresponding FVE radii, become smaller with decreasing vibrational frequency. In PS and

https://dx.doi.org/10.1021/jacs.0c13397
J. Am. Chem. Soc. 2021, 143, 3583−3594

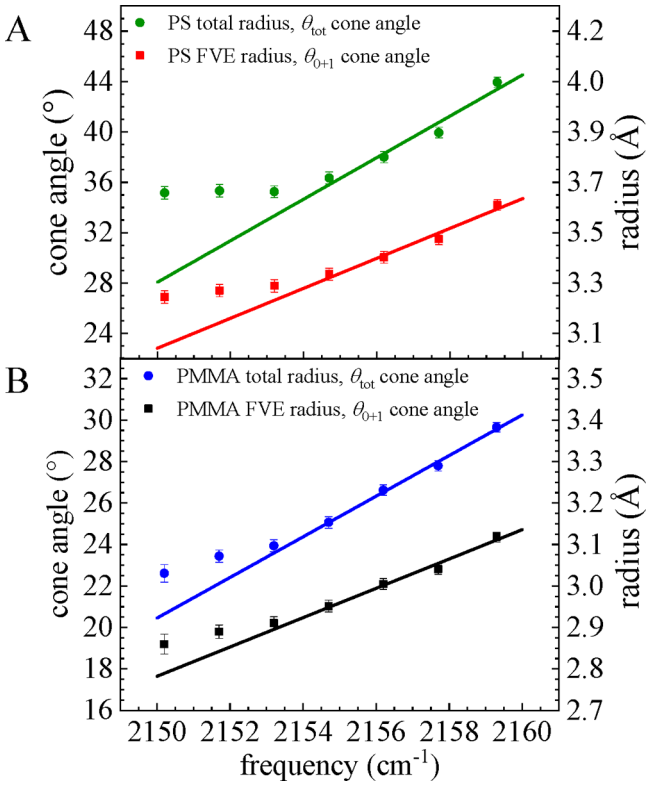

Figure 3. Frequency-dependent cone angles and their associated FVE radii for (A) PS and (B) PMMA. Left axis: cone angles obtained from eq 4. Right axis: corresponding radii obtained from eq 5. θ_{0+1} (red and black points) and associated radii (r_{0+1}) are the FVEs cone angles and sizes, while θ_{tot} and associated radii (r_{tot}) are the long-time measurements that reflect structural dynamics of the FVE shapes (see text). Solid lines are guides for the eye to show the linear dependence at high frequencies and the deviation from linearity at low frequencies. Deviation from linearity is more pronounced in PS than in PMMA. Error bars are for the cone angles as determined with eq 4.

PMMA, the high-frequency regime displays a linear relationship between frequency and FVE radius. However, in the lower frequency regime, there is a departure from linearity that is substantially more pronounced in PS than in PMMA (solid lines indicate the linear relationship). In Figure 3A, the low-frequency regime in PS shows the FVE radii level off to an almost constant value. In PS, the deviation from a Gaussian begins closer to the peak of the absorption spectrum compared to PMMA (Figure 1). This results in a more pronounced deviation from linearity for PS in Figure 3A (red points) than for PMMA (Figure 3B, black points). As will be described in Section 3.2, this deviation from linearity is associated with a highly non-Gaussian distribution of FVE radii in PS and to a lesser extent in PMMA.

3.1.3. Vibrational Stark Effect for Calculating Local Electric Fields. The first-order vibrational Stark effect is used to map the probe's vibrational frequencies to local electric field amplitudes.[25,43,47] The details of this model have been presented previously.[25] For a first-order vibrational Stark effect, the frequency shift experienced by a vibrational mode is

$$\omega = \omega_0 + \vec{F}.\frac{\vec{\mu}}{\hbar} \quad (6)$$

where ω is the observed vibrational frequency, ω_0 is the zero-field vibrational frequency, $\vec{\mu}$ is the dipole moment difference vector (Stark tuning parameter), and $\vec{F}$ is the local electric field. For a nitrile stretch, $\vec{\mu}$ is essentially along the CN bond.[25] $\vec{\mu}$ and ω_0 for the CN stretch in PhSeCN were previously determined from solvatochromic shifts in common solvents,[18] which in nitriles, has been shown to be a robust method.[25,43] ω_0 and $\vec{\mu}$ were found to be 2163.7 ± 1.5 cm^{-1} and 12.3 ± 2.4 cm^{-1}/(GV/m), respectively. These parameters enable frequency-dependent local electric fields to be determined and associated with specific FVE sizes. While PhSeCN has a large permanent dipole (~4 D) and the local electric fields are large (on the order of GV/m), it was shown that the tendency of the dipole to align with the local field is small and does not affect the interpretation of the results of the pump−probe measurements.[18]

The reduction in the change in radius with frequency at low frequencies (Figure 3) means that the correlation of electric field with the measured radius breaks down for small FVE radii, particularly in PS. Figure 4 shows the electric field

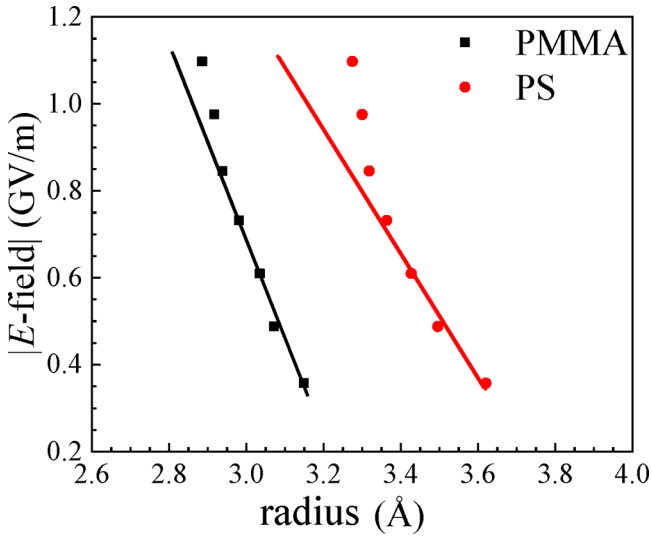

Figure 4. Electric field strengths (GV/m) in the FVE interiors experienced by vibrational probes as a function of FVE radius in PS (red) and PMMA (black). The PMMA data display a close-to-linear trend across the spectrum, while the PS data show a significant departure from linearity in the small FVE radius regime. Solid lines are guides for the eye.

strength for each FVE radius obtained using eq 6. These data show that at the higher frequencies (larger radii, Figure 3) there is a linear relationship between the radius and the electric field. However, this relationship becomes weak, particularly for PS, at small radii. A given electric field is associated with a larger radius in PS than in PMMA. For example, an *E*-field of 0.6 GV/m in PMMA corresponds to a radius of 3.0 Å, while the same *E*-field in PS corresponds to a radius of 3.4 Å. The three highest electric field points (lowest frequencies) in PS have almost the same FVE radii. Since the electric field arises from the particular polymer structure around the probe molecule, it follows that a single FVE radius can result from a large number of different polymer configurations. These observations indicate that small FVEs display a broader distribution of polymer structural configurations than larger FVEs, particularly in PS. For larger radii (higher frequency) the

https://dx.doi.org/10.1021/jacs.0c13397
J. Am. Chem. Soc. 2021, 143, 3583−3594

substantial change in *E*-field with radius indicates that there is a narrow distribution of structures that give rise to a particular FVE radius. These observations are supported by molecular dynamics simulations (see SI) and are discussed below.

3.2. Calculating the FVE Size Probability Distributions. The measured radius at each frequency can be related to a probability distribution of FVE radii. This process was performed in the prior ROAM publication studying PMMA by assuming a simple relationship between the cumulative distribution functions (CDFs) for the frequency probability distribution, $\rho(\omega)$, and the FVE radii distribution, $\rho(r)$:

$$\int_0^{\omega} \rho(\omega)\, \mathrm{d}\omega = \int_0^{r(\omega)} \rho(r)\, \mathrm{d}r \tag{7}$$

where r is the measured FVE radius and ω is the frequency of the probing molecule.[18] The above equality is true if the measured FVE radii are monotonic in frequency and there is a one-to-one correspondence between FVE radius and frequency (the conditional probability $\rho(r|\omega)$ is a Dirac delta function). However, the PS measurements presented in Figure 3 show that the measured radii over a range of low frequencies are nearly identical, which means that at least some radii can produce multiple frequencies. eq 7 was unable to account for the new behavior observed in PS, nor was it applicable to PMMA, which was clear after more the complete data presented in this paper were acquired. The new experimental observations demonstrated that the previous mathematical description of the FVE radii distribution is not general and probably not applicable to any polymer system. Therefore, a general approach, not based on a linear relationship between the FVE radius and the spectral frequency (see high-frequency data points in Figure 3B), was developed to describe the distribution of FVE radii.

The ROAM observable (Figure 3) is the average radius of the FVEs for a particular frequency of the probe molecule's CN stretch. This can be expressed as an expectation value

$$\langle r(\omega)\rangle = \frac{1}{\rho(\omega)} \int_0^{\infty} \rho(\omega|r)\rho(r) r\, \mathrm{d}r \tag{8}$$

where $\rho(r)$ is the desired FVE distribution, $\rho(\omega)$ is the probability distribution of probe frequencies (area normalized FT-IR absorption spectrum), $\rho(\omega|r)$ is a conditional probability density function (PDF) corresponding to the probability of a probe having frequency ω given it is in an FVE of radius r (the absorption spectrum of the sub-ensemble PhSeCN in FVEs of a particular radius). Section E in the SI presents a detailed description of the derivation of eq 8, as well as of the methodology employed to determine the appropriate $\rho(\omega|r)$ and $\rho(r)$.

Briefly, since $\rho(\omega)$ and $\langle r(\omega)\rangle$ are experimentally measured (Figures 1 and 3, respectively), the behavior of $\rho(\omega|r)$ is first chosen and used to derive a corresponding $\rho(r)$ that reproduces the absorption spectrum. The choice of $\rho(\omega|r)$ is iterated to obtain a set of $\rho(\omega|r)$ and $\rho(r)$ which also reproduces the measured FVE radii. Requiring the fits to simultaneously reproduce both observables greatly constrains the results.

In determining $\rho(\omega|r)$, we assume the $\rho(\omega|r)$ PDFs are Gaussian, with radius-dependent center frequencies and standard deviations. Figure 3 shows that for both PMMA and PS, a significant step in frequency at high frequencies corresponds to a significant change in radius. The deviation from this behavior for small radii measured at low frequency requires a non-linear relationship between radius and frequency.[18] To account for this non-linear behavior, the model used to determine $\rho(\omega|r)$ has the standard deviation of the frequency associated with a particular radius increase with decreasing radii.

For comparison, another model is discussed in the SI. In the model that is employed (referred to as Model 2, see SI), the standard deviation of the spectral line associated with a measured radius at a particular frequency increases as the FVE radius becomes small. This choice is based on initial molecular dynamics simulations (see SI) of the orientational dynamics of PhSeCN in a PS oligomer (5 repeat units). Oligomer simulations are useful because the simulation system can be properly equilibrated. Orientational dynamics for the oligomer slightly above its glass transition temperature display frequency-dependent behavior (Figure S8) that is qualitatively very similar to that displayed by the high-molecular-weight polymers below T_g shown in Figure 2. The simulations quantitatively reproduce the experimental anisotropy decay (Figure S9). The complete details of these experiments and simulations on several molecular weight oligomers will be presented subsequently. Here, we only use the simulations results to demonstrate the appropriateness of the model used for the calculations of $\rho(r)$.

The simulations show an increase in the range of electric fields associated with a particular radius as the radius becomes smaller (Figure S10). Because the electric field determines the frequency via the first-order Stark effect, as r_{0+1} (FVE radius) becomes small, an increase in the electric field's standard deviation corresponds to an increased spectral standard deviation. This is precisely the basis for the model used as discussed in connection with the fits shown in Figure 5. The model indicates that there are more polymer structures that can give rise to an FVE with a particular radius as the radius becomes smaller. Different polymer structures give rise to different electric fields. Then, more structural configurations will produce a wider range of electric fields, and therefore, a broader spectrum (larger standard deviation) associated with a sub-ensemble of particular radius.

The results of applying the model to the relationship between the FVE (r_{0+1}) radii in PS and the frequency are presented in Figure 5. The center frequencies of $\rho(\omega|r)$ varied at least linearly with FVE radius, and as discussed above, the standard deviation grew with decreasing radius. The joint distribution, $\rho(\omega,r) = \rho(\omega|r)\rho(r)$ is presented in Figure 5A. The black points are the experimental radii vs frequency, and the red line is the calculated average radii vs frequency from eq 8. The agreement between the experimental data and the calculated curve is excellent. The amplitude of the contour plot describes the probability of a probe molecule having a given frequency and being in an FVE of a given size, and horizontal slices show the distribution of frequencies associated with a particular radius. It can be seen that the spectral standard deviation (width of a horizontal slice) increases as the radius becomes smaller. The PS experimental FT-IR spectrum (black dashed curve) and the calculated spectrum (red curve) are shown in Figure 5B. The agreement between the experimental and calculated spectra is very good. Figure 5 shows that the experimental data, i.e., the radii and the non-Gaussian absorption spectrum, can be reproduced quantitatively. The analogous calculations for PMMA, which yield equally good results, are given in the SI.

https://dx.doi.org/10.1021/jacs.0c13397
J. Am. Chem. Soc. 2021, 143, 3583−3594

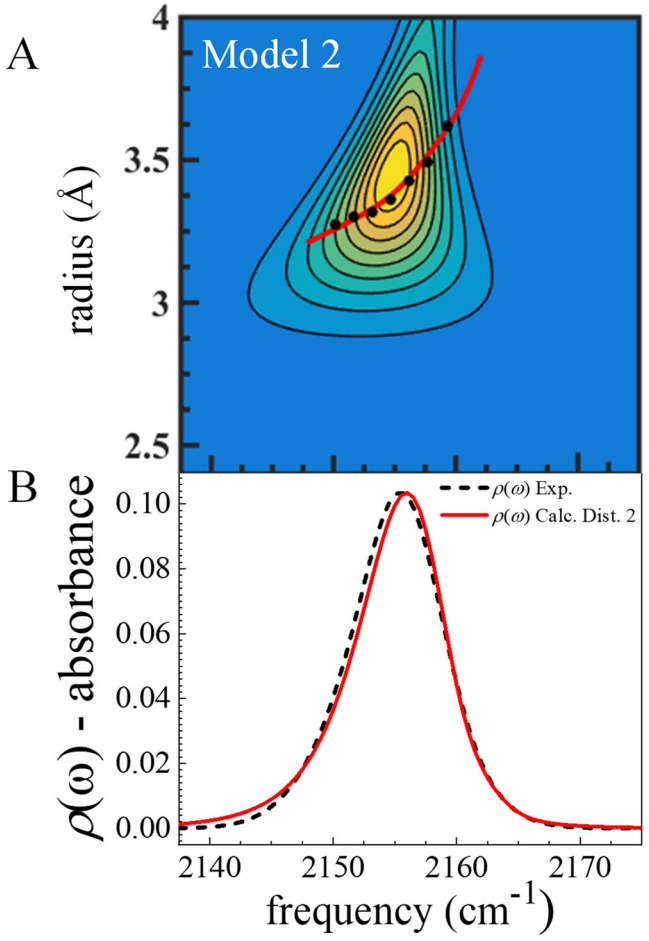

Figure 5. Results of the maximum entropy calculation for the FVE size distribution of PS. The maximum entropy calculations are required to simultaneously fit the frequency-dependent radii data and the probe's absorption spectrum. The calculations reproduce both the frequency-dependent FVE radii and the FT-IR spectrum with excellent agreement. (A) Joint probability distributions of FVE radius and probe frequency, $\rho(\omega,r)$. The black points are the measured radii vs frequency and the solid red curve is the calculated radii vs frequency. (B) The experimental FT-IR spectrum (black dashed curve) and the calculated spectrum. The model used for the calculations is supported by molecular dynamics simulations (see SI).

Figure 6 displays the area-normalized probability density functions for the FVE radii (r_{0+1}) of PS and PMMA. The dashed lines in the figure are the average radii with values of 3.0 and 3.4 Å for PMMA and PS, respectively. The results obtained from the ROAM analysis show that PS has larger FVE radii than PMMA, as well as a broader size distribution. The peaks of the PDF are at 2.94 and 3.29 Å for PMMA and PS, respectively, which results from the substantial fraction of small radii that are observed on the red side of the spectra. The averages are very close to the peaks of the distributions. For both polymers, the curves to the small r sides of the peaks are virtually perfect Gaussians. Both polymer distributions are non-Gaussian on the large r side of their peaks, with tails extending to large radius. The tails arise from the larger radii experimentally observed on the blue side of the spectra. The PS PDF has a substantially longer tail extending to large r than PMMA. The FWHM of the distributions are 0.40 and 0.57 Å for PMMA and PS, respectively. Therefore, PS has a broader

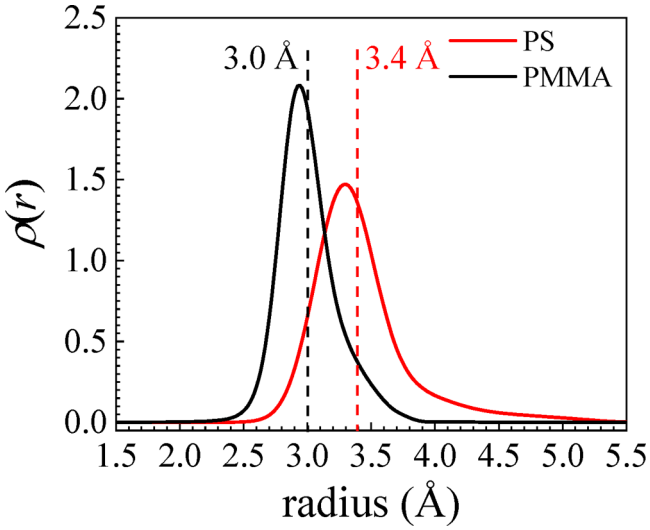

Figure 6. Area-normalized probability density functions, $\rho(r)$, for FVE radii in PS (red) and PMMA (black). Both polymers have a non-Gaussian $\rho(r)$, but the effect is much more pronounced in PS than in PMMA. The small radius rising edge of both curves are essentially perfect Gaussians, but both polymers have tails to large radius. The tail to large radius is much more pronounced for PS.

distribution of FVE radii, which extends further from the peak to large FVE size than PMMA.

3.3. Comparison to Other Studies. Positron Annihilation Lifetime Spectroscopy (PALS) is the standard method for the measurement of FVE sizes in a variety of materials, including amorphous glassy polymers.[26] PALS determines the FVE radius by bombarding a polymer glass sample with positrons. Ortho-positronium (o-Ps) is formed, which preferentially localizes in the polymer FVEs.[4,26,27] Within a few nanoseconds, the positron in the o-Ps annihilates with an electron from the surrounding polymer.[26,27] By treating an FVE as a spherical pore with a particular electron density and layer thickness at the pore surface, the o-Ps lifetime determines the radius of the FVE using the Tao−Eldrup equation.[4,26,32] PALS does not measure time dependent properties of the polymer system. It cannot determine the extent of time dependence of FVE shape fluctuations as discussed in connection with Figure 3. Therefore, the PALS measurements are most analogous to the ROAM r_{0+1} results.

PALS and ROAM report average FVE radii that are of similar size. PALS reports average radii for both PMMA and PS of 2.8 Å, essentially indistinguishable from each other.[4,5] However, other reports give average FVE radii values of 2.6 and 2.9 Å for PMMA and PS, respectively, showing variations among different PALS studies.[1] By contrast, ROAM reports average radii of 3.0 Å for PMMA and 3.4 Å for PS. Previously, we reported the average FVE radius of PMMA as 3.1 Å.[18] We determined that the difference was caused by residual solvent in the polymer film (see SI). As discussed above and in the SI, detailed concentration studies were performed to ensure that the concentration of residual solvent was sufficiently low not to affect the measurements. Probe concentration studies were also performed (see SI), which demonstrate that the concentration was sufficiently low such that the results did not depend on the probe concentration.

A possible source for the differences between the PALS and ROAM measurements is that the PALS analysis generally neglects polymer-dependent chemical interactions of the

https://dx.doi.org/10.1021/jacs.0c13397
J. Am. Chem. Soc. 2021, 143, 3583−3594

matrix with the *o*-Ps species.[26] These interactions have been shown to be significant in a limited number of systems, which include, for example, polymers with strongly electron withdrawing atoms.[48] However, a full systematic study of the impact of these interactions for different materials has been recognized as an active area of PALS research and a complete understanding of its behavior is currently unavailable.[26] The present PALS literature then implicitly suggests that all polymer structures have identical interactions with the *o*-Ps probe, that is, identical electron density at the surface of the model spherical pore. A larger electron density will increase the overlap integral between the wavefunctions of the *o*-Ps and the electrons on the inner wall of the FVE, thus shortening the *o*-Ps lifetime, and causing a decrease in the measured FVE radii. PS, with electron rich phenyl groups, would be expected to have a higher electron density than PMMA.

MD simulations have also been performed to predict the FVE size distribution as measured by PALS in a polystyrene matrix at 298 K.[49] It was concluded that the assumptions employed in PALS result in an underestimation of the FVE size distribution of PS, and reports an average radius more similar to the ROAM result. However, as an identical analysis has not been performed on PMMA, it is not possible to make an equivalent comparison. It should be emphasized that despite the entirely different experimental methods and the large difference in sizes of the *o*-Ps and PhSeCN probes (*o*-Ps is half the size of a hydrogen 1s wavefunction), ROAM and PALS report FVE radii that are at most a few tenths of an angstrom different. The agreement between the ROAM and the PALS results demonstrate that the PhSeCN probe is not influencing the sizes of the FVEs on which it reports.

It has been recognized in the literature that, provided a particular gas does not participate in specific gas-polymer interactions, an increase in gas permeability is correlated with larger FVE radii in the polymer matrix.[1,50] Oxygen is one such gas, which has no particular affinity for either PS or PMMA. The diffusion constant, D, for O_2 is $(1-4) \times 10^{-7}$ cm^2/s in PS and $(1-4) \times 10^{-8}$ cm^2/s in PMMA,[51−53] while its solubility constant, S, is 7.8×10^{-3} mol/(L atm) in PS and 8.7×10^{-3} mol/(L atm) in PMMA.[52,53] It follows that O_2 permeability, P, in PS (2.3−2.9 Barrer) is greater than in PMMA (0.09−0.3 Barrer), and it is attributed to the large increase in O_2 diffusivity.[1,51]

It is important to note that gas diffusivity is favored by the interconnectedness of a polymer's FVEs. In general, greater interconnectedness of FVEs does not necessarily mean that the FVEs are larger, although for a particular polymer matrix volume, larger FVEs could result in their boundaries being closer to one another, which could increase gas diffusivity. It is also likely that the FVE time-dependent shape and center position fluctuations play an important role in gas diffusion. While these macroscopic results do not directly measure the size of FVEs, they do suggest that, consistent with the ROAM results, the FVEs in PS are larger than those in PMMA.

Solvent permeation studies have also shown that the permeation constant of methyl ethyl ketone through PS and PMMA is 1.1×10^4 and 1.06 nm s^{-1}, respectively.[54] This large difference in permeation rates also suggests that PS has larger FVEs than PMMA.

PMMA and PS have both also been investigated using a photochromic photoisomerization technique and through the introduction of a second harmonic generation (SHG) aromatic system into their matrices.[6,34,55] These results suggest that PMMA may have larger FVEs than PS, which is in direct contrast to ROAM measurements, some of PALS results, and gas permeation studies. However, the probes used in photoisomerization and SHG measurements are considerably larger than those used in ROAM and PALS. The volume required for photoisomerization of the smallest probe used is on the order of the average FVE size reported by ROAM. It has been previously observed in the literature that different methods report different FVE sizes in the same polymer matrices,[6,18,32,34] and that the size of the probe can influence the measurement.[56] The probe size will determine which FVEs it can populate, and which ones the probe is too large to enter.[56] Therefore, in the context of experimental techniques, a further distinction between the total free volume and the volume accessible to the probe—free accessible volume (FAV)—is necessary. The large probe sizes in the photochromic and SHG experiments are likely to produce large differences in the FAV sampled, preferentially sampling pores large enough to accept the probe molecules. The sizes of these probes are found only on the large radius end of the FVE distributions sampled by ROAM and PALS; FVEs too small to accept these large probes remain unexplored. Additionally, these techniques do not directly measure the FVE sizes, but provide an indirect method of determining what fraction of the FVEs in the FAV are larger than the probe used. Due to the many fundamental differences between these techniques and ROAM, and their different observables, a direct comparison of the results is not possible.

4. CONCLUDING REMARKS

We have applied and extended the recently developed Restricted Orientation Anisotropy Method (ROAM)[18] for the determination of free volume element (FVE) sizes, size probability density functions (PDFs), and FVE dynamics for PS and PMMA. ROAM uses ultrafast IR anisotropy measurements on a small probe molecule. The probe molecule's orientational relaxation is restricted by the size of the FVE in which it is located. The measurements determine the range of angles that the probe can sample, and based on this angular cone and the size of the probe, the FVE radii are determined. Measurements at different IR frequencies across the probe's inhomogeneously broadened vibrational absorption spectrum provided different cone angles, and therefore different FVE radii. The measurements across the IR spectrum allowed the distribution of FVE radii to be determined and the PDF to be obtained. The model used to determine the PDFs required simultaneous calculations to reproduce both the measured radii and the IR absorption spectrum (see Figures 5 and 6). The underlying physical assumptions of the model that yields the PDFs was supported by molecular dynamics simulations, which are detailed in the SI. In addition to FVE sizes, dynamics, and the PDFs, the electric fields as a function of FVE radius were determined via a first-order Stark effect analysis (see Figure 4).

The ROAM results showed that PS has larger FVE radii and a broader size distribution than PMMA. Using the measured results to determine the FVE PDF, the sizes range from 2.4 to 3.9 Å in PMMA, and between 2.6 and 5.4 Å in PS, with average FVE radii of 3.0 and 3.4 Å in PMMA and PS, respectively. Our measurements show differences from previous studies of FVEs in PMMA and PS.[4,5,32,34,55] However, these studies are in disagreement with each other. Our PMMA vs PS results are

https://dx.doi.org/10.1021/jacs.0c13397
J. Am. Chem. Soc. 2021, 143, 3583−3594

consistent with macroscopic studies of gas and solute diffusivity in the two polymer matrices.[S0−S4]

In addition to the FVE sizes and the PDF, ROAM provides information on the structural dynamics of the FVEs. The FVE radii are determined from the cone angles θ_{0+1}, which yield r_{0+1}. The total cone angles, θ_{tot}, give different sizes, r_{tot}, which are larger than the FVE radii. As discussed in detail previously,[18] the larger cones and radii reflect the extent of FVE shape fluctuations. The FVE shape fluctuates through the motions of side groups and small chain segments, but the average size of a sub-ensemble of FVEs with a particular r_{0+1} does not change. The shape fluctuations for both PS and PMMA occur on a similar time scale of ∼150 ps. Side groups or small chain segments can move into FVEs while other moieties move out, but the size, on average, remains the same. However, new angular space has been opened for the probe to sample, producing a larger total cone angle and the associated larger r_{tot}. The shape fluctuations could also result in fluctuations of the centers of the FVEs about their average positions. While the FVEs do not displace, the relatively fast fluctuations in shape and position may be important in processes like electron transport and gas permeability.

In addition to FVE sizes and time-dependent shape fluctuations, the ROAM measurements on PS and PMMA using the CN stretch of the probe PhSeCN also gave the size dependent electric fields via the first-order Stark effect.[18] The electric field determines the frequency of the CN absorption. On the blue side of the IR absorption spectrum (large FVEs), the size is well correlated with the frequency and therefore the electric field. On the red side of the line (small FVEs), a given radius is associated with a broad range of frequencies, and therefore, a broad range of electric fields. These measurements have important implications for the nature of the structures of FVEs. The electric field within an FVE, as experienced by the probe's Stark shift, arises from the distribution of partial charges on the polymer in the FVE. Different electric fields will arise from different configurations of the polymer chains and side groups. As the size of the FVEs becomes smaller, the results show that there is an increasing number of distinct local polymer configurations that can result in a particular FVE radius. This phenomenon is more pronounced in PS than in PMMA. The fact that there is a more limited range of polymer configurations that can give rise to large FVEs is responsible for the PDF peaking at the small end of the size distribution.

The results presented in this paper demonstrate that ROAM is a powerful technique for investigating the characteristics and behavior of polymer FVEs. This technique provides insight into the time-dependent character and electrostatic properties of FVEs, and it is sensitive to sub-angstrom differences across different polymer structures. In addition, ROAM is a non-destructive technique, as the sample is unchanged by the measurement. Therefore, it is well-suited for characterizing structural changes over arbitrarily long time scales. For example, it should be very useful in correlating the effects of polymer aging on properties such as dielectric breakdown and gas permeability, by studying the FVE size distribution and dynamics over periods of days and months. Additionally, the structural and dynamic characteristics of a polymer film can be measured pre- and post-electrical stressing. Changes in the distribution of sizes, intrinsic electric fields, and FVE dynamics can be of particular importance, as such measurements may be able to elucidate the reason that electric field aging leads to a reduction in a polymer's intrinsic breakdown electric field.

■ ASSOCIATED CONTENT

Supporting Information

The Supporting Information is available free of charge at https://pubs.acs.org/doi/10.1021/jacs.0c13397.

Additional discussion, Figures S1−S12, and Tables S1−S5, related to NMR spectroscopy, orientational dynamics and FVE radii as functions of solvent content, PhSeCN population lifetime decay, parameterization of orientational relaxation dynamics, calculating the FVE size probability distributions, the polystyrene oligomer, molecular dynamics simulations, and maximum entropy distributions for PS and PMMA (PDF)

■ AUTHOR INFORMATION

Corresponding Author

Michael D. Fayer − *Department of Chemistry, Stanford University, Stanford, California 94305, United States;* orcid.org/0000-0002-0021-1815; Email: fayer@stanford.edu

Authors

Sebastian M. Fica-Contreras − *Department of Chemistry, Stanford University, Stanford, California 94305, United States;* orcid.org/0000-0003-4177-8436

David J. Hoffman − *Department of Chemistry, Stanford University, Stanford, California 94305, United States;* orcid.org/0000-0001-8518-7676

Junkun Pan − *Department of Chemistry, Stanford University, Stanford, California 94305, United States*

Chungwen Liang − *Computational Modeling Core Facility, Institute for Applied Life Sciences, University of Massachusetts Amherst, Amherst, Massachusetts 01003, United States;* orcid.org/0000-0001-9721-6411

Complete contact information is available at: https://pubs.acs.org/10.1021/jacs.0c13397

Notes

The authors declare no competing financial interest.

■ ACKNOWLEDGMENTS

This work was supported by Office of Naval Research Grant N00014-17-1-2656. We would like to thank Dr. Stephen Lynch for assistance at the Stanford NMR facility. S.M.F.-C. would like to thank John P. Breen for assistance with the infrared laser system.

■ REFERENCES

(1) Yampolskii, Y. P. Methods for investigation of the free volume in polymers. *Russ. Chem. Rev.* **2007**, *76* (1), 59−78.

(2) Low, Z. X.; Budd, P. M.; McKeown, N. B.; Patterson, D. A. Gas Permeation Properties, Physical Aging, and Its Mitigation in High Free Volume Glassy Polymers. *Chem. Rev.* **2018**, *118* (12), 5871−5911.

(3) Jansen, J. C.; Macchione, M.; Tocci, E.; De Lorenzo, L.; Yampolskii, Y. P.; Sanfirova, O.; Shantarovich, V. P.; Heuchel, M.; Hofmann, D.; Drioli, E. Comparative Study of Different Probing Techniques for the Analysis of the Free Volume Distribution in Amorphous Glassy Perfluoropolymers. *Macromolecules* **2009**, *42* (19), 7589−7604.

(4) Liu, J.; Deng, Q.; Jean, Y. C. Free-Volume Distributions of Polystyrene Probed by Positron Annihilation: Comparison with Free-Volume Theories. *Macromolecules* **1993**, *26* (26), 7149−7155.

(5) Wästlund, C.; Maurer, F. H. J. Positron Lifetime Distributions and Free Volume Parameters of PEO/PMMA Blends Determined with the Maximum Entropy Method. *Macromolecules* **1997**, *30* (19), 5870−5876.
(6) Royal, J. S.; Victor, J. G.; Torkelson, J. M. Photochromic and Fluorescent Probe Studies in Glassy Polymer Matrices. 4. Effects of Physical Aging on Poly(methyl methacrylate) As Sensed by a Size Distribution of Photochromic Probes. *Macromolecules* **1992**, *25*, 729−734.
(7) Turnbull, D.; Cohen, M. H. Free-Volume Model of the Amorphous Phase: Glass Transition. *J. Chem. Phys.* **1961**, *34* (1), 120−125.
(8) Cohen, M. H.; Turnbull, D. Molecular Transport in Liquids and Glasses. *J. Chem. Phys.* **1959**, *31* (5), 1164−1169.
(9) Chow, T. S. Kinetics of Free Volume and Physical Aging in Polymer Glasses. *Macromolecules* **1984**, *17* (11), 2336−2340.
(10) Hasan, O. A.; Boyce, M. C.; Li, X. S.; Berko, S. An Investigation of the Yield and Postyield Behavior and Corresponding Structure of Poly(methyl methacrylate). *J. Polym. Sci., Part B: Polym. Phys.* **1993**, *31* (2), 185.
(11) O'Connor, K. M.; Scholsky, K. M. Free volume effects on the melt viscosity of low molecular weight poly(methyl methacrylate). *Polymer* **1989**, *30* (3), 461−466.
(12) Greiner, R.; Schwarzl, F. R. Thermal contraction and volume relaxation of amorphous polymers. *Rheol. Acta* **1984**, *23*, 378−395.
(13) Knauss, W. G.; Emri, I. J. Non-linear viscoelasticity based on free volume consideration. *Comput. Struct.* **1981**, *13* (1−3), 123−128.
(14) Artbauer, J. Electric strength of polymers. *J. Phys. D: Appl. Phys.* **1996**, *29* (2), 446−456.
(15) White, R. P.; Lipson, J. E. G. Free Volume in the Melt and How It Correlates with Experimental Glass Transition Temperatures: Results for a Large Set of Polymers. *ACS Macro Lett.* **2015**, *4* (5), 588−592.
(16) White, R. P.; Lipson, J. E. G. Polymer Free Volume and Its Connection to the Glass Transition. *Macromolecules* **2016**, *49* (11), 3987−4007.
(17) Robertson, R. E. Segmental mobility in the equilibrium liquid below the glass transition. *Macromolecules* **1985**, *18* (5), 953−958.
(18) Hoffman, D. J.; Fica-Contreras, S. M.; Fayer, M. D. Amorphous polymer dynamics and free volume element size distributions from ultrafast IR spectroscopy. *Proc. Natl. Acad. Sci. U. S. A.* **2020**, *117* (25), 13949−13958.
(19) Royal, J. S.; Torkelson, J. M. Photochromic and Fluorescent Probe Studies in Glassy Polymer Matrices. 5. Effects of Physical Aging on Bisphenol-A Polycarbonate and Poly(vinyl acetate) As Sensed by a Size Distribution of Photochromic Probes. *Macromolecules* **1992**, *25* (18), 4792−4796.
(20) Galizia, M.; Chi, W. S.; Smith, Z. P.; Merkel, T. C.; Baker, R. W.; Freeman, B. D. 50th Anniversary Perspective: Polymers and Mixed Matrix Membranes for Gas and Vapor Separation: A Review and Prospective Opportunities. *Macromolecules* **2017**, *50* (20), 7809−7843.
(21) Tan, H.-S.; Piletic, I. R.; Fayer, M. D. Polarization selective spectroscopy experiments: methodology and pitfalls. *J. Opt. Soc. Am. B* **2005**, *22* (9), 2009−2017.
(22) Lipari, G.; Szabo, A. Model-Free Approach to the Interpretation of Nuclear Magnetic Resonance Relaxation in Macromolecules. 1. Theory and Range of Validity. *J. Am. Chem. Soc.* **1982**, *104* (17), 4546−4559.
(23) Tan, H. S.; Piletic, I. R.; Fayer, M. D. Orientational dynamics of water confined on a nanometer length scale in reverse micelles. *J. Chem. Phys.* **2005**, *122* (17), 174501.
(24) Lipari, G.; Szabo, A. Effect of Libration Motion on Fluorescence Depolarization and Nuclear Magnetic Resonance Relaxation in Macromolecules and Membranes. *Biophys. J.* **1980**, *30* (3), 489−506.
(25) Levinson, N. M.; Fried, S. D.; Boxer, S. G. Solvent-induced infrared frequency shifts in aromatic nitriles are quantitatively described by the vibrational Stark effect. *J. Phys. Chem. B* **2012**, *116* (35), 10470−6.
(26) Jean, Y. C.; Van Horn, J. D.; Hung, W.-S.; Lee, K.-R. Perspective of Positron Annihilation Spectroscopy in Polymers. *Macromolecules* **2013**, *46* (18), 7133−7145.
(27) Liao, K.-S.; Chen, H.; Awad, S.; Yuan, J.-P.; Hung, W.-S.; Lee, K.-R.; Lai, J.-Y.; Hu, C.-C.; Jean, Y. C. Determination of Free-Volume Properties in Polymers Without Orthopositronium Components in Positron Annihilation Lifetime Spectroscopy. *Macromolecules* **2011**, *44* (17), 6818−6826.
(28) Félix, M. V.; Consolati, G.; Velázquez, R.; Castaño, V. M. Positron annihilation studies of nanoholes and microphase formation control of a PMMA+MMA+TEGDMA system. *Polymer* **2006**, *47* (1), 265−271.
(29) Hofmann, D.; Entrialgo-Castano, M.; Lerbret, A.; Heuchel, M.; Yampolskii, Y. Molecular Modeling Investigation of Free Volume Distributions in Stiff Chain Polymers with Conventional and Ultrahigh Free Volume: Comparsion between Molecular Modeling and Positron Lifetime Studies. *Macromolecules* **2003**, *36* (22), 8528−8538.
(30) Li, H.-L.; Ujihira, Y.; Nanasawa, A.; Jean, Y. C. Estimation of free volume in polystyrene-polyphenylene ether blend probed by the positron annihilation lifetime technique. *Polymer* **1999**, *40* (2), 349−355.
(31) Shantarovich, V. P.; Azamatova, Z. K.; Novikov, Y. A.; Yampolskii, Y. P. Free-Volume Distribution of High Permeability Membrane Materials Probed by Positron Annihilation. *Macromolecules* **1998**, *31* (12), 3963−3966.
(32) Ban, M.; Kyoto, M.; Uedono, A.; Kawano, T.; Tanigawa, S. Free Volumes in Polystyrene Probed by Positron Annihilation. *J. Polym. Sci., Part B: Polym. Phys.* **1996**, *34* (7), 1189−1195.
(33) Yu, Z.; Yahsi, U.; McGervey, J. D.; Jamieson, A. M.; Simha, R. Molecular Weight-Dependence of Free Volume in Polystyrene Studied by Position Annihilation Measurements. *J. Polym. Sci., Part B: Polym. Phys.* **1994**, *32* (16), 2637−2644.
(34) Victor, J. G.; Torkelson, J. M. Photochromic and Fluorescent Probe Studies in Glassy Polymer Matrices. 3. Effects of Physical Aging and Molar Weight on the Size Distribution of Local Free Volume in Polystyrene. *Macromolecules* **1988**, *21* (12), 3490−3497.
(35) Victor, J. G.; Torkelson, J. M. On Measuring the Distribution of Local Free Volume in Glassy Polymers by Photochromic and Fluorescence Techniques. *Macromolecules* **1987**, *20* (9), 2241−2250.
(36) Nagasaka, B.; Eguchi, T.; Nakayama, H.; Nakamura, N.; Ito, Y. Positron annihilation and ^{129}Xe NMR studies of free volume in polymers. *Radiat. Phys. Chem.* **2000**, *58*, 581−585.
(37) Yan, C.; Thomaz, J. E.; Wang, Y. L.; Nishida, J.; Yuan, R.; Breen, J. P.; Fayer, M. D. Ultrafast to Ultraslow Dynamics of a Langmuir Monolayer at the Air/Water Interface Observed with Reflection Enhanced 2D IR Spectroscopy. *J. Am. Chem. Soc.* **2017**, *139* (46), 16518−16527.
(38) Karthick Kumar, S. K.; Tamimi, A.; Fayer, M. D. Comparisons of 2D IR measured spectral diffusion in rotating frames using pulse shaping and in the stationary frame using the standard method. *J. Chem. Phys.* **2012**, *137* (18), 184201.
(39) Hoffman, D. J.; Fica-Contreras, S. M.; Pan, J.; Fayer, M. D. Pulse-shaped chopping: Eliminating and characterizing heat effects in ultrafast infrared spectroscopy. *J. Chem. Phys.* **2020**, *153* (20), 204201.
(40) Tokmakoff, A. Orientational correlation functions and polarization selectivity for nonlinear spectroscopy of isotropic media. I. Third order. *J. Chem. Phys.* **1996**, *105* (1), 1−12.
(41) Hoffman, D. J.; Sokolowsky, K. P.; Fayer, M. D. Direct observation of dynamic crossover in fragile molecular glass formers with 2D IR vibrational echo spectroscopy. *J. Chem. Phys.* **2017**, *146* (12), 124505.
(42) Bian, H.; Wen, X.; Li, J.; Zheng, J. Mode-specific intermolecular vibrational energy transfer. II. Deuterated water and potassium selenocyanate mixture. *J. Chem. Phys.* **2010**, *133* (3), 034505.

https://dx.doi.org/10.1021/jacs.0c13397
J. Am. Chem. Soc. 2021, 143, 3583−3594

(43) Bagchi, S.; Fried, S. D.; Boxer, S. G. A solvatochromic model calibrates nitriles' vibrational frequencies to electrostatic fields. *J. Am. Chem. Soc.* **2012**, *134* (25), 10373−6.
(44) Kramer, P. L.; Giammanco, C. H.; Fayer, M. D. Dynamics of water, methanol, and ethanol in a room temperature ionic liquid. *J. Chem. Phys.* **2015**, *142* (21), 212408.
(45) Moilanen, D. E.; Fenn, E. E.; Lin, Y.-S.; Skinner, J. L.; Bagchi, B.; Fayer, M. D. Water inertial reorientation: Hydrogen bond strength and the angular potential. *Proc. Natl. Acad. Sci. U. S. A.* **2008**, *105* (14), 5295−5300.
(46) Wang, C. C.; Pecora, R. Time-correlation functions for restricted rotational diffusion. *J. Chem. Phys.* **1980**, *72* (10), 5333−5340.
(47) Andrews, S. S.; Boxer, S. G. Vibrational Stark Effects of Nitriles II. Physical Origins of Stark Effects from Experiment and Perturbation Theory. *J. Phys. Chem. A* **2002**, *106* (3), 469−477.
(48) Sato, K.; Murakami, H.; Ito, K.; Hirata, K.; Kobayashi, Y. Positron and Positronium Annihilation in Polymers Studied by Age-Momentum Correlation Spectroscopy. *Acta Phys. Pol., A* **2008**, *113* (5), 1511.
(49) Schmitz, H.; Müller-Plathe, F. Calculation of the lifetime of positronium in polymers via molecular dynamics simulations. *J. Chem. Phys.* **2000**, *112* (2), 1040−1045.
(50) Shieh, Y.-T.; Liu, K.-H. Solubility of CO_2 in Glassy PMMA and PS over a Wide Pressure Range: The Effect of Carbonyl Groups. *J. Polym. Res.* **2002**, *9*, 107−113.
(51) Peterson, C. M. Permeability Studies on Heterogeneous Polymer Films. *J. Appl. Polym. Sci.* **1968**, *12* (12), 2649−2667.
(52) Poulsen, L.; Ogilby, P. R. Oxygen Diffusion in Glassy Polymer Films: Effects of Other Gases and Changes in Pressure. *J. Phys. Chem. A* **2000**, *104* (12), 2573−2580.
(53) Charlesworth, J. M.; Gan, T. H. Kinetics of Quenching of Ketone Phosphorescence by Oxygen in a Glassy Matrix. *J. Phys. Chem.* **1996**, *100* (36), 14922−14927.
(54) Coll, H.; Searles, C. G. Solvent permeation rates and ageing phenomena in polymer coatings. *Polymer* **1988**, *29* (7), 1266−1272.
(55) Hampsch, H. L.; Yang, J.; Wong, G. K.; Torkelson, J. M. Orientation and Second-Harmonic Generation in Doped Polystyrene and Poly(methyl methacrylate) Films. *Macromolecules* **1988**, *21* (2), 526−528.
(56) Ronova, I. A.; Rozhkov, E. M.; Alentiev, A. Y.; Yampolskii, Y. P. Occupied and Accessible Volumes in Glassy Polymers and Their Relationship with Gas Permeation Parameters. *Macromol. Theory Simul.* **2003**, *12* (6), 425−439.

https://dx.doi.org/10.1021/jacs.0c13397
J. Am. Chem. Soc. 2021, 143, 3583−3594